Research Square

Preprints are preliminary reports that have not undergone peer review.
They should not be considered conclusive, used to inform clinical practice,
or referenced by the media as validated information.

All-electrical Coherent Control of a Single Rare-earth Spin Qubit

Fabio Donati

donati.fabio@qns.science

IBS Center for Quantum Nanoscience https://orcid.org/0000-0002-3932-2889

Yaowu Liu

IBS Center for Quantum Nanoscience

Dasom Choi

IBS Center for Quantum Nanoscience https://orcid.org/0009-0001-8013-8629

Stefano Reale

QuTech and Kavli Institute of Nanoscience, Delft University of Technology

Jeongmin Oh

Center for Quantum Nanoscience, Institute for Basic Science https://orcid.org/0009-0009-8852-3028

Seorhin Choi

IBS Center for Quantum Nanoscience

Lei Fang

IBS Center for Quantum Nanoscience

We-hyo Soe

IBS Center for Quantum Nanoscience

Arzhang Ardavan

University of Oxford https://orcid.org/0000-0001-5521-2658

Andreas Heinrich

Institute for Basic Science at Ewha Womans University https://orcid.org/0000-0001-6204-471X

Soo-hyon Phark

Institute for Basic Science https://orcid.org/0000-0002-0541-5083

Article

Keywords:

Posted Date: August 12th, 2026

DOI: https://doi.org/10.21203/rs.3.rs-10423711/v1

License: This work is licensed under a Creative Commons Attribution 4.0 International License.
Read Full License

Additional Declarations: There is **NO** Competing Interest.

All-electrical Coherent Control of a Single Rare-earth Spin Qubit

Yaowu Liu,[1,2,*†] Dasom Choi,[1,3,*] Stefano Reale,[1,2,*] Jeongmin Oh,[1,3]
Seorhin Choi,[1,3] Lei Fang,[1,2] We-hyo Soe,[1,2] Arzhang Ardavan,[4]
Andreas J. Heinrich,[1,3] Soo-hyon Phark,[1,2,‡] and Fabio Donati[1,3,§]

[1]*Center for Quantum Nanoscience (QNS),*
Institute for Basic Science (IBS), Seoul 03760, Republic of Korea
[2]*Ewha Womans University, Seoul 03760, Republic of Korea*
[3]*Department of Physics, Ewha Womans University, Seoul 03760, Republic of Korea*
[4]*Department of Physics, University of Oxford,*
The Clarendon Laboratory, Oxford OX1 3PU, U.K

Abstract

Electrical control of single spin qubits is a major frontier for nanoscale, high-speed, and scalable quantum devices. Yet, extending it to highly shielded rare-earth $4f$ electrons remains an experimental challenge across solid-state platforms. Here we demonstrate all-electrical coherent control of a single Er electron spin, which is exchange-coupled to a nearby Ti atom. Scanning tunneling microscopy-based electron spin resonance with three-dimensional magnetic-field control enables comprehensive mapping of the resonance and Rabi frequencies, revealing pronounced anisotropies in both the Er $\mathfrak{g}$-tensor and the Er-Ti exchange interaction. The electrical modulation of the anisotropic Er-Ti coupling results in an efficient drive of the Er spin, allowing us to achieve near-gigahertz Rabi frequencies – a ten-fold improvement over the present record for rare-earth spin qubits. By establishing anisotropic exchange as a general resource for electrically accessing shielded rare-earth spins, our results open a new route to ultrafast and local control of rare-earth spins in solid-state quantum devices.

I. INTRODUCTION

Rare-earth $4f$-electron spins provide a versatile platform for quantum technologies, including spin qubits[1–6], optical quantum memories[2,3,7,8], and single-photon sources[9,10]. Among them, erbium (Er) stands out for its optically addressable ground state, making it highly promising as a spin qubit for spin-photon interfaces at telecom wavelengths[2–6,11–15]. While single-ion optical control of rare-earth qubits has seen remarkable recent progress[16–22], electrical control offers a scalable route toward dense integration and ultrafast gate operations[23–25].

Despite demonstrations in bulk crystals and molecular systems[1,19,26,27], achieving electrical coherent control of an individual rare-earth spin remains a fundamental challenge, arising from the strong shielding of the $4f$ orbitals by outer shells, which severely limits the transduction of external electric fields into effective driving fields of $4f$ spins. A mediator spin that is both electrically addressable and precisely coupled to the rare-earth atom is therefore required[28,29], but engineering such a mediator with the required precision is difficult in conventional solid-state and molecular platforms.

Atomic spins on surfaces provide a powerful platform for precisely engineering such mediator interactions[30–32], offering identical qubits with atom-by-atom addressability[33] and bottom-up designability via scanning-probe control[34,35], as well as tunability in charge and spin states[36,37]. When combining scanning tunneling microscopy with electron spin resonance (ESR-STM), this platform further enables coherent manipulation and readout of a single spin with atomic precision[28,29,33,38]. Despite recent advances in the readout of single rare-earth atoms, for example, by exploiting partially filled $6s$ shells[37] or coupling to a nearby sensor spin[12], coherent electrical manipulation of an individual rare-earth spin still remains elusive.

Here we exploit a tailored Er-Ti spin pair on an MgO/Ag(100) surface, where the contrasting $\mathfrak{g}$-tensor anisotropies of Er and Ti cause the two coupled spins to respond differently to the oscillating electric field, generating an effective transverse driving field on the Er spin tunable by the magnetic field direction. We achieve a near-gigahertz Rabi frequency, a record for rare-earth spin qubits, and identify a general mechanism for electrical coherent control based on the effective wobbling of coupled magnetic moments.

II. REMOTE DRIVE OF A SINGLE Er SPIN

Here we implement interaction-mediated driving of a single rare-earth spin, in which electrical excitation of a neighboring spin is transduced into an effective transverse magnetic field acting on the target spin. To realize this concept, we engineer a tailored Er-Ti spin pair on an MgO/Ag(100) surface (Methods), as shown in the scanning tunneling microscopy (STM) topography image in Fig. 1**a** and schematic in Fig. 1**b**. The design combines an Er atom occupying a low-symmetry binding site on the MgO surface, namely an oxygen-oxygen bridge site [Er(B)], with exchange coupling $\mathcal{J}$ to a nearby Ti atom. This low-symmetry binding site gives Er a strongly anisotropic magnetic moment ($\boldsymbol{\mu}_{\mathrm{Er}}$, Fig. 1**b**). As a result, the Ti spin generates an effective exchange field on Er ($\boldsymbol{B}_{\mathcal{J}} \propto \boldsymbol{\mu}_{\mathrm{Ti}}\mathcal{J}$). Under RF electric excitation, modulation of this exchange field produces a transverse driving field ($\boldsymbol{B}_1 \propto \delta\boldsymbol{B}_{\mathcal{J}}$), enabling coherent control of the Er spin (Fig. 1**b**). The pair is assembled by atom manipulation[39] (Fig. 1**a**), with Er and Ti separated by three surface lattice sites along the oxygen-to-oxygen (O-O) direction. Taking advantage of this geometry, we define the x-axis along the O-O direction, the y-axis perpendicular to it, and the z-axis along the surface normal, corresponding to the pair geometry $(3, 0)$, as shown in Fig. 1**a**.

Erbium adsorbed at a bridge site of the MgO surface, denoted hereafter as Er unless otherwise specified, shows neither spin excitations in tunneling spectroscopy nor ESR signals when addressed directly (Supplementary Section I). This behavior is consistent with the absence of unpaired $5d$ and $6s$ electrons, similar to Er atoms adsorbed at oxygen sites [Er(O)][12]. In contrast, when the STM tip is positioned over the Ti atom of the Er-Ti pair and an RF electric field is applied, five ESR transitions are observed, as shown in Fig. 1**c**. The four lower frequency peaks can be divided into two groups (f_1, f_2 and f_3, f_4), showing the same splitting ($f_2 - f_1$ and $f_4 - f_3$) of a few hundred MHz, which reflects the Er-Ti spin-spin interaction strength. The relative amplitudes of the two transitions in each group reveal an antiferromagnetic spin-spin coupling[40]. Similar to the Er(O)-Ti case, the eigenstates of the Er(B)-Ti spin pair form a four-level manifold: $|00\rangle$, $|11\rangle$, $|+\rangle = \cos(\eta/2)\,|01\rangle + \sin(\eta/2)\,|10\rangle$, and $|-\rangle = \sin(\eta/2)\,|01\rangle - \cos(\eta/2)\,|10\rangle$, where $\tan(\eta) = |\mathcal{J}|/\delta$ and δ is the Zeeman-energy detuning between the two spins. We ascribe the above four ESR peaks to the four single quantum transitions (SQT, f_1 to f_4, Fig. 1**d**). The fifth transition (f_5) appears at twice the mean frequency of the four single quantum transitions (Fig. 1**d** and Supplementary Section

II), and it is related to a double quantum transition (DQT) in which both Er and Ti spins are rotated simultaneously[12].

III. FAST COHERENT CONTROL OF $4f$ ELECTRONS

First, we applied a nearly in-plane magnetic field ($\boldsymbol{B}_{\text{ext}} = 0.25$ T, $\theta = 83°$) at an azimuthal angle of $\phi = 52°$ that maximizes the intensity of the single-quantum transitions (Fig. 1**c**). Under this field orientation, the system eigenstates are tuned to be approximately product states in the Zeeman basis (Supplementary Section IV): $|+\rangle \approx |\widetilde{01}\rangle$ and $|-\rangle \approx |\widetilde{10}\rangle$, as shown in Fig. 1**d**. The response of each peak to the magnetic field from the spin-polarized tip reveals that the transitions f_3 and f_1 are dominated by the Er and Ti spin resonances, respectively (Supplementary Section V).

We performed Rabi measurements on the transition f_3, yielding coherent oscillations (Fig. 2**a**) with a Rabi frequency of 190 MHz, which is one order of magnitude higher than the previously reported record for Er-based qubits in solid-state platforms[41]. In stark contrast, the Rabi sequence measured on an isolated Ti atom shows only weak oscillations (Fig. 2**a**) with a Rabi frequency of 19 MHz, an order of magnitude lower than that of the Er transition. Such a high Rabi frequency is observed exclusively from the Er spin transition (f_3) and not the case for the Ti transition (f_1) or the DQT (f_5) in the pair (Figs. 2**c** and **d**, red and purple squares), which remain similar to that of the isolated Ti atom under the same conditions. The Rabi frequencies for all transitions scale linearly with the applied RF voltage V_{RF} (Fig. 2**d**), confirming that the oscillations arise from coherent RF-driven spin rotations. Notably, the slope for the Er transition f_3 is about an order of magnitude larger than those of the Ti SQT and DQT, highlighting the strongly enhanced driving efficiency of the Er $4f$ spin. This enhanced driving efficiency identifies the Er $4f$ spin as a compelling platform for electrically controlled spin qubits on surfaces.

A further interesting feature is the independence of the Er f_3 Rabi frequencies on the tunneling conductance (Fig. 2**e**), i.e., the tip-Ti distance, excluding the role of $\boldsymbol{B}_{\text{tip}}$ in the coherent driving of the Er spin. In contrast, the Rabi frequency of the Ti transition f_1 in the pair initially increases with decreasing tip-Ti distance, consistent with an enhanced tip-induced driving field[29], and then saturates (Fig. 2**e**, red squares; see also Supplementary Section VI).

We note that coherent control of the DQT is of particular interest for applications in quantum entanglement[42,43] and quantum sensing[44], but has not been demonstrated previously for surface atoms. The DQT requires the coherent rotation of both Er and Ti spins, which suggests the coherent control mechanism is related to the spin-spin interaction, as further discussed in the following section.

To survey the influence of the spin pair geometry, i.e., atomic separation and pair orientation, on the Rabi frequency, we prepared two more distinct Er-Ti pairs of surface lattice coordinate configurations, (3.5, 0.5) and (2.5, −0.5), as depicted in Fig. 3**a**, and performed ESR measurements for a comparative study with the (3, 0) pair. ESR spectra taken at the same magnetic field reveal a clear monotonic increase in the splitting between the transitions f_1 and f_2 with decreasing separation (Fig. 3**b**, colored arrows), consistent with the expected distance dependence of the spin-spin interaction. By contrast, the Rabi frequencies of the Er transitions show an interesting behavior (Figs. 3**c** and **d**), markedly increasing from (3.5, 0.5) to (3, 0), however does not show a particular change by a further decrease of separation. This suggests a nontrivial correlation between spin-spin interaction and driving strength, which will be explained in the following section. The coherence times of the Er transitions in these pairs are on the order of 100 ns, possibly limited by the lifetime of the Ti spin[33] (Supplementary Section VII).

IV. MAGNETIC ANISOTROPY OF Er-Ti SPIN PAIR

From the data presented in Figs. 2 and 3, it is clear that the effective transverse driving field $\boldsymbol{B}_1$ acting on the Er spin does not originate from the tip field, and it is not only related to the magnitude of the spin-spin interaction. To provide a detailed model, we reconstructed the static Hamiltonian for the Er-Ti (3, 0) pair by taking advantage of our three-dimensional control of the magnetic field at a fixed magnitude. We first measured the ESR transition energies as a function of magnetic-field polar angle θ while the azimuthal angle ϕ was fixed at 52° (Fig. 4**a**). The first transition group (f_1, f_2) remains nearly unchanged at around 6 GHz, reflecting almost isotropic couplings (i.e. $\mathfrak{g}$-tensor) of the spins to the external field in this field-rotation plane. The weak anisotropy in these transition energies suggests that these transitions are mainly related to the Ti spin[38,40,45], confirming the results deduced from the tip-field dependence. By contrast, the second group (f_3, f_4) shows a substantial

increase in the transition energy, indicating a significantly anisotropic $\mathfrak{g}$-tensor of the spin that dominates these transitions. Their intensities decrease when the field rotates away from the in-plane direction ($\theta = 90°$) and eventually smear out with the field along the surface normal (see Fig. 5**d**), suggesting the driving is significantly influenced by the field direction.

Similarly, rotating the magnetic field within the surface plane reveals a pronounced angular dependence of the ESR spectra, with all four transitions exhibiting substantial shifts in frequency across the range of 5 - 9 GHz (Fig. 4**b**). This behavior indicates a strong in-plane $\mathfrak{g}$-tensor anisotropy of Er and highlights the tunable eigenstates using the field orientation. Notably, when the field is aligned with the principal crystallographic axes ($\phi = 0°$ and 90°), the transitions f_3 and f_4 become completely unobservable (Fig. S16), reflecting a pronounced angular selectivity of the allowed ESR transitions. Of particular interest, the interaction strength between the two spins, extracted from the splitting between f_1 and f_2 (or f_3 and f_4, Fig. 1**c**), shows a pronounced change with the angle ϕ. This indicates an anisotropic exchange interaction, which, to our knowledge, has not previously been observed in other on-surface spin systems.

To interpret these experimental observations, we map the Er ground-state doublet onto an effective spin of $S = 1/2$ ($\boldsymbol{S}_{\mathrm{Er}}$) and construct a spin Hamiltonian for the Er-Ti pair:

$$\mathcal{H} = -\mu_{\mathrm{B}} \boldsymbol{S}_{\mathrm{Ti}} \cdot \mathfrak{g}^{\mathrm{Ti}} \cdot (\boldsymbol{B}_{\mathrm{ext}} + \boldsymbol{B}_{\mathrm{tip}}) - \mu_{\mathrm{B}} \boldsymbol{S}_{\mathrm{Er}} \cdot \mathfrak{g}^{\mathrm{Er}} \cdot \boldsymbol{B}_{\mathrm{ext}} + \boldsymbol{S}_{\mathrm{Ti}} \cdot \mathcal{J} \cdot \boldsymbol{S}_{\mathrm{Er}}, \tag{1}$$

where μ_{B} is the Bohr magneton, $\boldsymbol{B}_{\mathrm{ext}}$ is the external magnetic field, $\boldsymbol{B}_{\mathrm{tip}}$ is the magnetic field from the spin-polarized tip, $\mathfrak{g}^{\mathrm{Ti}}$ and $\mathfrak{g}^{\mathrm{Er}}$ are the $\mathfrak{g}$-tensors of Ti and Er, respectively, and $\mathcal{J}$ is the effective interaction tensor, including both exchange ($\mathcal{J}^{\mathrm{exc}}$) and dipolar contributions (Supplementary Section III). As in previous works, the effective tip field $\boldsymbol{B}_{\mathrm{tip}}$ only applies to the spin under the tip, in this case Ti[40].

Considering the symmetry of the Er-Ti pair given by the adsorption sites, only diagonal components of $\mathfrak{g}^{\mathrm{Er}}$ and $\mathcal{J}$ are non-zero. The experimental data, including transition intensities and Rabi frequencies described later, are well reproduced by taking $\boldsymbol{B}_{\mathrm{tip}}$ as a free parameter (solid curves in Figs. 4**a** and **b**; Supplementary Section III). Using the known $\mathfrak{g}^{\mathrm{Ti}}$ tensor[46], the fit yields $\mathfrak{g}^{\mathrm{Er}}_{xx} = 1.05 \pm 0.02$, $\mathfrak{g}^{\mathrm{Er}}_{yy} = 2.22 \pm 0.02$, and $\mathfrak{g}^{\mathrm{Er}}_{zz} = 9.59 \pm 0.04$, revealing a strong anisotropy of the Er(B) magnetic moment with an out-of-plane easy axis (Fig. 4**c**). The two-fold symmetry of the oxygen-bridge binding site also leads to different g factors along the two in-plane directions, in contrast to the case of Er(O)[12,47]. In addition, the fit

yields the exchange components of $\mathcal{J}^{\rm exc}_{xx} = 79.6 \pm 5.5$ MHz, $\mathcal{J}^{\rm exc}_{yy} = 543.7 \pm 6.3$ MHz, and $\mathcal{J}^{\rm exc}_{zz} = 1272.5 \pm 7.8$ MHz. The pronounced anisotropy in both $\mathcal{J}^{\rm exc}$ and $\mathfrak{g}^{\rm Er}$ originates from the combined effects of strong spin-orbit coupling (SOC) and the crystal-field potential under the reduced symmetry of Er(B)[48]. These anisotropies are therefore distinct from those of Er(O), owing to the different ligand fields at the two binding sites. For Er(O), the quantum states are split in an almost uniaxial ligand field provided by the oxygen atom underneath. By contrast, atomic multiplet calculations of Er(B) (Supplementary Section VIII) combined the electrostatic potential of O/Mg atoms together with the occupation of the $5d_{y^2}$ orbital, elongated along the y-axis (i.e., perpendicular to O-O direction), to impose an out-of-plane easy axis for Er(B). The calculated principal values of $\mathfrak{g}$-tensor, as shown in Fig. 4**c** (solid lines) qualitatively agree with the experimental results.

V. COHERENT CONTROL MECHANISM

Using the parameters obtained from the fits in Section II.**B**, we now turn to the mechanism generating the driving field $\boldsymbol{B}_1$ for such large Rabi frequencies shown in Section II.**A**. Based on the finding that the $\boldsymbol{B}_1$ acting on the Er spin depends not only on the separation but also on the orientation of an Er-Ti pair (Fig. 3), we write the spin-pair interaction $\mathcal{J}(\boldsymbol{q})$ using a generalized vector of three variables $\boldsymbol{q} = (\boldsymbol{r}, \boldsymbol{\eta}_{\rm Ti}, \boldsymbol{\eta}_{\rm Er})$: $\boldsymbol{r}$, the vector connecting two spins, and $\boldsymbol{\eta}_{\rm Ti(Er)}$, the orientations of Ti (Er) orbitals in the ground state of the pair with respect to the lattice.

Our model is as follows: an RF drive results in the time-dependence of $\mathcal{J}$: $\mathcal{J}(\boldsymbol{q} + \delta\boldsymbol{q}(t))$ and generates non-zero off-diagonal components, together with the diagonal components in $\mathcal{J}$ (Supplementary Section IX). We first tried to simulate ESR spectroscopy of the spin pair only by modulating the diagonal components, which fails to describe the experimental trends (Figs. S9-S11). By contrast, simulations using the off-diagonal terms successfully reproduce all the experimental ESR transitions and the dependence of their intensities on the magnetic field angles (Fig. 5**b**). In general, $\mathcal{J}(\boldsymbol{q}+\delta\boldsymbol{q}(t))$ depends on the trajectory of $\boldsymbol{q}(t)$ (Supplementary Section IX). To minimize the energetic cost of the RF excitation, we consider the rotational trajectory that leaves the dominant Zeeman energy unchanged. Physically, the RF electric field modulates the orbital structure that defines the principal axes of the $\mathfrak{g}$-tensor and the exchange tensor $\mathcal{J}^{\rm exc}$. Through spin-orbit coupling, this modulation can

be equivalently described as a wobbling of the magnetic moments around the external field, $\boldsymbol{B}_{\text{ext}}$ (Fig. 5**a** and Fig. S12):

$$\mathcal{H}_1 = \boldsymbol{S}_{\text{Ti}} \left[\hat{R}_{\text{B}}^T(\delta\alpha) \mathcal{J} \hat{R}_{\text{B}}(\delta\alpha) - \mathcal{J} \right] \boldsymbol{S}_{\text{Er}} = \delta\alpha \boldsymbol{S}_{\text{Ti}} \left[\mathcal{J}, G \right] \boldsymbol{S}_{\text{Er}} \tag{2}$$

where $\hat{R}_{\text{B}}(\delta\alpha)$ is the $SO(3)$ rotational operator around $\boldsymbol{B}_{\text{ext}}$; G is the generator of $\hat{R}_{\text{B}}(\delta\alpha)$ and $\delta\alpha(t) = \delta\alpha_0 \cos\omega_{\text{RF}} t$ represents the infinitesimal angular modulation of magnetic moments induced by the RF excitation. Note that this mechanism is only valid for anisotropic $\mathcal{J}$ and a more general formula taking into account the $\mathfrak{g}$-tensor anisotropy is given in Supplementary Section IX and the Methods section.

Using the driving term in Eq. (2), we calculate Rabi frequencies in the spin pair as shown in Fig. 5**c** for the transitions f_3 (Er-like transition) and f_5 (DQT). Their dependence on the field direction (θ, ϕ) reveals strong anisotropies. The Rabi frequencies in both transitions are enhanced when an in-plane field is applied, but show an opposite ϕ-dependence, e.g., maximum for f_3 and minimum for f_5 at $\phi \sim 50°$ (marked by the red star). We further simulate the ESR spectra at $\phi = 52°$ with a varying θ for all five transitions and compare with the experimental data (Fig. 5**b**, Supplementary Section X). In Fig. 5**d**, we take a careful look at the θ-dependence of the ESR intensities for f_3 and f_5, showing excellent agreement between simulations and experiments.

The angular maps in Fig. 5**c** allow us to intuitively grasp the coherent manipulation mechanism in our spin pair: The Rabi frequency vanishes (Fig. 5**c**) along the two in-plane lattice directions ($\theta = 90°$; $\phi = 0°$ or $90°$), clearly supporting the vanishing ESR intensity in the experiments (Fig. S16). The magnetic moments of both spins ($\boldsymbol{\mu}_{\text{Er}}$, $\boldsymbol{\mu}_{\text{Ti}}$) in this case are fully aligned with the field (see schemes with triangular and circular markers in Fig. 5**a**), preventing their rotational modulations. As ϕ deviates from $0°$ or $90°$, neither $\boldsymbol{\mu}_{\text{Er}}$ nor $\boldsymbol{\mu}_{\text{Ti}}$ is aligned with the external field due to the anisotropies of their $\mathfrak{g}$-tensors. Here we note the much stronger in-plane anisotropy of the Er $\mathfrak{g}$-tensor than that of Ti, leading to deviation of Er quantization axis toward the y-direction, which is much more pronounced than that of Ti (Figs. 1**b** and 5**a**). Therefore, the rotational modulation of $\boldsymbol{\mu}_{\text{Ti}}$ produces an effective transverse field $\boldsymbol{B}_1$ along the out-of-plane direction, which couples to $\mathfrak{g}_{\text{zz}}^{\text{Er}}$ and generates the Rabi coupling. As we found in Fig. 4, the surprisingly large $\mathfrak{g}_{\text{zz}}^{\text{Er}} = 9.59$, thus explains the strong Rabi frequency of the Er transition (f_3) (also see Fig. S17). However, the mixture of rotation along x and y directions at this angle accidentally depletes the Rabi coupling of

the DQT, also in good agreement with the experiments (Fig. 5**c**).

Our model also reproduces the angular dependence of the SQT, DQT, and the Rabi frequencies, measured from the (2.5, −0.5) pair (Fig. 3; Supplementary Section IX, Fig. S14). Compared to the (3, 0) pair, the magnitude of the Er-Ti coupling is larger overall. However, the Rabi frequency does not increase substantially because it is governed by the pair direction as well as the anisotropic nature of $\mathcal{J}$ (Supplementary Section IX). In addition, our model predicts a Rabi frequency that is approximately 30 times smaller for the Er(O)-Ti pair, owing to the predominantly isotropic exchange coupling (see Supplementary Section XI, Figs. S19, S20), hence explaining the lack of coherent oscillations in the Er(O)-Ti pair within the range of the experimental control parameters[12].

VI. DISCUSSION AND OUTLOOK

Our demonstration of all-electrical coherent control and readout of both the Er spin and the DQT highlights rare-earth atoms on surfaces as a promising platform for atom-scale spin-based quantum devices. The atom-by-atom addressability and tunable spin-spin interactions enable a bottom-up design strategy that is difficult to realize in other solid-state qubit architectures. The high Rabi frequency, reaching up to 190 MHz, allows coherent manipulation on timescales well below the coherence limit, providing access to high-speed quantum gates and strong-drive regimes for exploring nonlinear and higher-order spin dynamics.

Moreover, we identify a general strategy that transduces electrical excitations into an effective coherent rotation of the rare-earth spin. This mechanism, relying on the anisotropic exchange interaction in coupled spins, not only enables ultra-fast manipulation of rare-earth spins, but also illustrates a broadly transferable design strategy for efficiently driven spin qubits in other scalable platforms. For example, such a strategy could directly benefit rare-earth ions in solids, which already combine long coherence times with optical interfaces[2–6], as well as semiconductor spin qubits[24,25,49,50], opening new opportunities for high-fidelity, versatile qubit architectures. Of particular interest, the coherent control mechanism we propose here may also serve as a design concept for molecular spin qubits[51–53] with high and tunable Rabi frequency, where the spin-spin interaction can be tailored through precise engineering of the chemical environment.

METHODS

A. Experiments

All STM measurements were conducted in a home-built low-temperature STM operated at 1.0 K[54], equipped with a three-axis magnet (1−4−6 T). The magnetic tip was made by picking up several Fe atoms from the MgO surface[55]. All data were taken at 1.0 K. Radio-frequency voltages (Keysight E8257D and E8267D) were applied to the junction through the tip. For time-resolved measurements, the pulse configuration was enabled by an Arbitrary Waveform Generator (Tektronix AWG 5400). The clocks were synchronized through the data acquisition system (NI USB-6200). For measurement with multiple RF pulses, the RF voltages were combined through a power splitter (Mini-Circuits ZC2PD-K0244++) and the pulse shapes were controlled by the Arbitrary Waveform Generator. The surface of a Ag(100) substrate was cleaned by repeated cycles of Ar^+ sputtering and annealing at ∼700 K. Ultrathin MgO(100) films were grown on Ag(100) by evaporating Mg metal in an oxygen atmosphere (10^{-6} Torr) with the sample kept at a temperature of ∼600 K[56]. Fe, Ti and Er atoms were deposited from high-purity rods (> 99%) using an e-beam evaporator at cryogenic temperature (∼ 10 K) to have well-isolated atoms on the surface.

B. Modeling

As established in Figs. 2 and 3 of the main text, the effective field acting on the Er spin depends not only on the Er-Ti distance, but also on the direction of the Er-Ti bond. We therefore describe the spin-spin interaction using an anisotropic exchange tensor,

$$\mathcal{H}_{\rm int} = \boldsymbol{S}_{\rm Ti}\mathcal{J}\boldsymbol{S}_{\rm Er}, \qquad \mathcal{J} = \mathcal{J}\left(\boldsymbol{q}\right). \tag{3}$$

Under RF excitation, the modulation of atomic orbitals for both spins can be represented as if the microscopic configuration $\boldsymbol{q}$ were weakly modulated along a trajectory $X_{\rm RF}(t)$. This covariant change can be written as the Lie derivative

$$\delta\mathcal{J}(t) = \mathcal{L}_{X_{\rm RF}(t)}\mathcal{J}, \tag{4}$$

with

$$\mathcal{L}_{X_{\rm RF}(t)}\mathcal{J} = X_{\rm RF}(t)\cdot\nabla\mathcal{J} + A_{\rm Ti}^{\mathsf{T}}(t)\mathcal{J} + \mathcal{J}A_{\rm Er}(t). \tag{5}$$

Here $A_{\mathrm{Ti}}(t)$ and $A_{\mathrm{Er}}(t)$ are infinitesimal generators associated with rotations of the Ti and Er local spin frames along the trajectory $X_{\mathrm{RF}}(t)$. The first term describes changes of the tensor components due to bond or orbital deformation, whereas the last two terms describe the rotation of the tensor indices. The ordinary derivative terms,

$$X_{\mathrm{RF}}(t) \cdot \nabla \mathcal{J} = \delta \boldsymbol{r}(t) \cdot \nabla_{\boldsymbol{r}} \mathcal{J} + \delta \boldsymbol{\eta}_{\mathrm{Ti}}(t) \cdot \nabla_{\boldsymbol{\eta}_{\mathrm{Ti}}} \mathcal{J} + \delta \boldsymbol{\eta}_{\mathrm{Er}}(t) \cdot \nabla_{\boldsymbol{\eta}_{\mathrm{Er}}} \mathcal{J}, \tag{6}$$

do not reproduce the observed angular dependence. We therefore focus on the rotational part of Eq. (5). For a finite angle rotation, this contribution can be expressed as

$$\mathcal{J} \rightarrow \mathcal{J}_{\mathrm{rot}}(t) = R_{\mathrm{Ti}}^{\mathsf{T}}(t) \mathcal{J} R_{\mathrm{Er}}(t), \tag{7}$$

and hence

$$\delta \mathcal{J}_{\mathrm{rot}}(t) = R_{\mathrm{Ti}}^{\mathsf{T}}(t) \mathcal{J} R_{\mathrm{Er}}(t) - \mathcal{J}. \tag{8}$$

The corresponding driving Hamiltonian under RF excitation is

$$\mathcal{H}_1(t) = \boldsymbol{S}_{\mathrm{Ti}} \delta \mathcal{J}_{\mathrm{rot}}(t) \boldsymbol{S}_{\mathrm{Er}}, \tag{9}$$

which is a more general form of Eq. (2). A more detailed description of the theory is provided in Supplementary Section IX.

ACKNOWLEDGMENT

The authors acknowledge support from Institute for Basic Science (grant: IBS-R027-D1). We thank Harald Brune, Nicolás Lorente, Chirstopher Lutz and Christoph Wolf for the stimulated discussions.

AUTHOR CONTRIBUTION

FD conceived the experiment. YL, DC, SR, JO, SP, and FD performed the experiments. YL and FD performed the modeling. FD and SC performed the multiplet calculations. YL, AJH, SP and FD wrote the manuscript with the input from all authors.

* These authors contribute equally.

† liu.yaowu@qns.science

‡ phark@qns.science

§ donati.fabio@qns.science

[1] S. Bertaina, S. Gambarelli, A. Tkachuk, I. Kurkin, B. Malkin, A. Stepanov, and B. Barbara, Nature Nanotechnology **2**, 39 (2007).

[2] M. Zhong, M. P. Hedges, R. L. Ahlefeldt, J. G. Bartholomew, S. E. Beavan, S. M. Wittig, J. J. Longdell, and M. J. Sellars, Nature **517**, 177 (2015).

[3] M. Rančić, M. P. Hedges, R. L. Ahlefeldt, and M. J. Sellars, Nature Physics **14**, 50 (2018).

[4] A. Ortu, A. Tiranov, S. Welinski, F. Fröwis, N. Gisin, A. Ferrier, P. Goldner, and M. Afzelius, Nature Materials **17**, 671 (2018).

[5] M. Le Dantec, M. Rančić, S. Lin, E. Billaud, V. Ranjan, D. Flanigan, S. Bertaina, T. Chanelière, P. Goldner, A. Erb, *et al.*, Science Advances **7**, eabj9786 (2021).

[6] M. Hiraishi, Z. H. Roberts, G. G. King, L. S. Trainor, and J. J. Longdell, Nature Physics **21**, 1112 (2025).

[7] M. P. Hedges, J. J. Longdell, Y. Li, and M. J. Sellars, Nature **465**, 1052 (2010).

[8] Y. Ma, Y.-Z. Ma, Z.-Q. Zhou, C.-F. Li, and G.-C. Guo, Nature Communications **12**, 2381 (2021).

[9] H. De Riedmatten, M. Afzelius, M. U. Staudt, C. Simon, and N. Gisin, Nature **456**, 773 (2008).

[10] A. Dibos, M. Raha, C. Phenicie, and J. D. Thompson, Physical Review Letters **120**, 243601 (2018).

[11] C. Benelli and D. Gatteschi, Chemical Reviews **102**, 2369 (2002).

[12] S. Reale, J. Hwang, J. Oh, H. Brune, A. J. Heinrich, F. Donati, and Y. Bae, Nature Communications **15**, 5289 (2024).

[13] S. Gupta, X. Wu, H. Zhang, J. Yang, and T. Zhong, Physical Review Applied **19**, 044029 (2023).

[14] S. Ourari, Ł. Dusanowski, S. P. Horvath, M. T. Uysal, C. M. Phenicie, P. Stevenson, M. Raha, S. Chen, R. J. Cava, N. P. de Leon, *et al.*, Nature **620**, 977 (2023).

[15] A. Sell, R. Scheu, A. Leitenstorfer, and R. Huber, Applied Physics Letters **93**, 251107 (2008).

[16] P. Siyushev, K. Xia, R. Reuter, M. Jamali, N. Zhao, N. Yang, C. Duan, N. Kukharchyk, A. Wieck, R. Kolesov, *et al.*, Nature Communications **5**, 3895 (2014).

[17] T. Zhong, J. M. Kindem, J. G. Bartholomew, J. Rochman, I. Craiciu, V. Verma, S. W. Nam, F. Marsili, M. D. Shaw, A. D. Beyer, *et al.*, Physical Review Letters **121**, 183603 (2018).

[18] J. M. Kindem, A. Ruskuc, J. G. Bartholomew, J. Rochman, Y. Q. Huan, and A. Faraon, Nature **580**, 201 (2020).

[19] M. Raha, S. Chen, C. M. Phenicie, S. Ourari, A. M. Dibos, and J. D. Thompson, Nature Communications **11**, 1605 (2020).

[20] S. Chen, M. Raha, C. M. Phenicie, S. Ourari, and J. D. Thompson, Science **370**, 592 (2020).

[21] M. T. Uysal, Ł. Dusanowski, H. Xu, S. P. Horvath, S. Ourari, R. J. Cava, N. P. De Leon, and J. D. Thompson, Physical Review X **15**, 011071 (2025).

[22] A. Gritsch, A. Ulanowski, J. Pforr, and A. Reiserer, Nature Communications **16**, 64 (2025).

[23] K. C. Nowack, F. H. Koppens, Y. V. Nazarov, and L. M. Vandersypen, Science **318**, 1430 (2007).

[24] F. N. Froning, L. C. Camenzind, O. A. van der Molen, A. Li, E. P. Bakkers, D. M. Zumbühl, and F. R. Braakman, Nature Nanotechnology **16**, 308 (2021).

[25] K. Wang, G. Xu, F. Gao, H. Liu, R.-L. Ma, X. Zhang, Z. Wang, G. Cao, T. Wang, J.-J. Zhang, *et al.*, Nature Communications **13**, 206 (2022).

[26] S. Thiele, F. Balestro, R. Ballou, S. Klyatskaya, M. Ruben, and W. Wernsdorfer, Science **344**, 1135 (2014).

[27] R. Vincent, S. Klyatskaya, M. Ruben, W. Wernsdorfer, and F. Balestro, Nature **488**, 357 (2012).

[28] J. Reina-Gálvez, H.-A. Le, H. T. Bui, S.-H. Phark, N. Lorente, and C. Wolf, Physical Review Research **7**, L042055 (2025).

[29] S.-H. Phark, H. T. Bui, A. Ferrón, J. Fernández-Rossier, J. Reina-Gálvez, C. Wolf, Y. Wang, K. Yang, A. J. Heinrich, and C. P. Lutz, Advanced Science **10**, 2302033 (2023).

[30] C. Wolf, A. J. Heinrich, and S.-H. Phark, ACS nano **18**, 28469 (2024).

[31] S.-H. Phark, B. Weber, Y. Yoshida, P. R. Forrester, R. J. Elbertse, J. A. Stroscio, H. Wang, K. Yang, L. Gross, S. Mishra, *et al.*, Nano Futures **9**, 032001 (2025).

[32] D.-J. Choi, S.-H. Phark, A. J. Heinrich, and N. Lorente, Nanoscale Advances **7**, 4551 (2025).

[33] Y. Wang, Y. Chen, H. T. Bui, C. Wolf, M. Haze, C. Mier, J. Kim, D.-J. Choi, C. P. Lutz, Y. Bae, *et al.*, Science **382**, 87 (2023).

[34] H. Wang, P. Fan, J. Chen, L. Jiang, H.-J. Gao, J. L. Lado, and K. Yang, Nature Nanotechnology **19**, 1782 (2024).

[35] K. Yang, S.-H. Phark, Y. Bae, T. Esat, P. Willke, A. Ardavan, A. J. Heinrich, and C. P. Lutz, Nature Communications **12**, 993 (2021).

[36] S.-H. Phark, H. T. Bui, W.-h. Seo, Y. Liu, V. Sheina, C. Lee, C. Wolf, A. J. Heinrich, R. Robles, and N. Lorente, Nature Communications (2026).

[37] G. Czap, K. Noh, J. Velasco Jr, R. M. Macfarlane, H. Brune, and C. P. Lutz, ACS Nano **19**, 3705 (2025).

[38] K. Yang, W. Paul, S.-H. Phark, P. Willke, Y. Bae, T. Choi, T. Esat, A. Ardavan, A. J. Heinrich, and C. P. Lutz, Science **366**, 509 (2019).

[39] D. M. Eigler and E. K. Schweizer, Nature **344**, 524 (1990).

[40] K. Yang, Y. Bae, W. Paul, F. D. Natterer, P. Willke, J. L. Lado, A. Ferrón, T. Choi, J. Fernández-Rossier, A. J. Heinrich, *et al.*, Physical Review Letters **119**, 227206 (2017).

[41] L. R. Weiss, G. T. Smith, R. A. Murphy, B. Golesorkhi, J. A. Méndez Méndez, P. Patel, J. Niklas, O. G. Poluektov, J. R. Long, and D. D. Awschalom, Science **390**, 76 (2025).

[42] F. Dolde, I. Jakobi, B. Naydenov, N. Zhao, S. Pezzagna, C. Trautmann, J. Meijer, P. Neumann, F. Jelezko, and J. Wrachtrup, Nature Physics **9**, 139 (2013).

[43] M. Morillas-Rozas, A. López-García, and J. Cerrillo, arXiv preprint arXiv:2501.18244 (2025).

[44] J. F. Barry, J. M. Schloss, E. Bauch, M. J. Turner, C. A. Hart, L. M. Pham, and R. L. Walsworth, Reviews of Modern Physics **92**, 015004 (2020).

[45] T. S. Seifert, S. Kovarik, D. M. Juraschek, N. A. Spaldin, P. Gambardella, and S. Stepanow, Science Advances **6**, eabc5511 (2020).

[46] J. Kim, W.-j. Jang, T. H. Bui, D.-J. Choi, C. Wolf, F. Delgado, Y. Chen, D. Krylov, S. Lee, S. Yoon, *et al.*, Physical Review B **104**, 174408 (2021).

[47] S. Reale, A. Singha, S. Ahmed, D. Krylov, L. Colazzo, C. Wolf, C. Casari, A. Barla, E. Fernandes, F. Patthey, *et al.*, Physical Review B **107**, 045427 (2023).

[48] V. Vieru, N. Iwahara, L. Ungur, and L. F. Chibotaru, Scientific Reports **6**, 24046 (2016).

[49] J. Van den Berg, S. Nadj-Perge, V. Pribiag, S. Plissard, E. Bakkers, S. Frolov, and L. P. Kouwenhoven, Physical Review Letters **110**, 066806 (2013).

[50] S. Geyer, B. Hetényi, S. Bosco, L. C. Camenzind, R. S. Eggli, A. Fuhrer, D. Loss, R. J. Warburton, D. M. Zumbühl, and A. V. Kuhlmann, Nature Physics **20**, 1152 (2024).

[51] A. Gaita-Ariño, F. Luis, S. Hill, and E. Coronado, Nature Chemistry **11**, 301 (2019).

[52] M. R. Wasielewski, M. D. Forbes, N. L. Frank, K. Kowalski, G. D. Scholes, J. Yuen-Zhou, M. A. Baldo, D. E. Freedman, R. H. Goldsmith, T. Goodson III, *et al.*, Nature Reviews Chemistry **4**, 490 (2020).

[53] K. S. Pedersen, A.-M. Ariciu, S. McAdams, H. Weihe, J. Bendix, F. Tuna, and S. Piligkos, Journal of the American Chemical Society **138**, 5801 (2016).

[54] J. Hwang, D. Krylov, R. Elbertse, S. Yoon, T. Ahn, J. Oh, L. Fang, W.-j. Jang, F. H. Cho, A. J. Heinrich, *et al.*, Review of Scientific Instruments **93**, 093703 (2022).

[55] S. Baumann, W. Paul, T. Choi, C. P. Lutz, A. Ardavan, and A. J. Heinrich, Science **350**, 417 (2015).

[56] W. Paul, K. Yang, S. Baumann, N. Romming, T. Choi, C. P. Lutz, and A. J. Heinrich, Nature Physics **13**, 403 (2017).

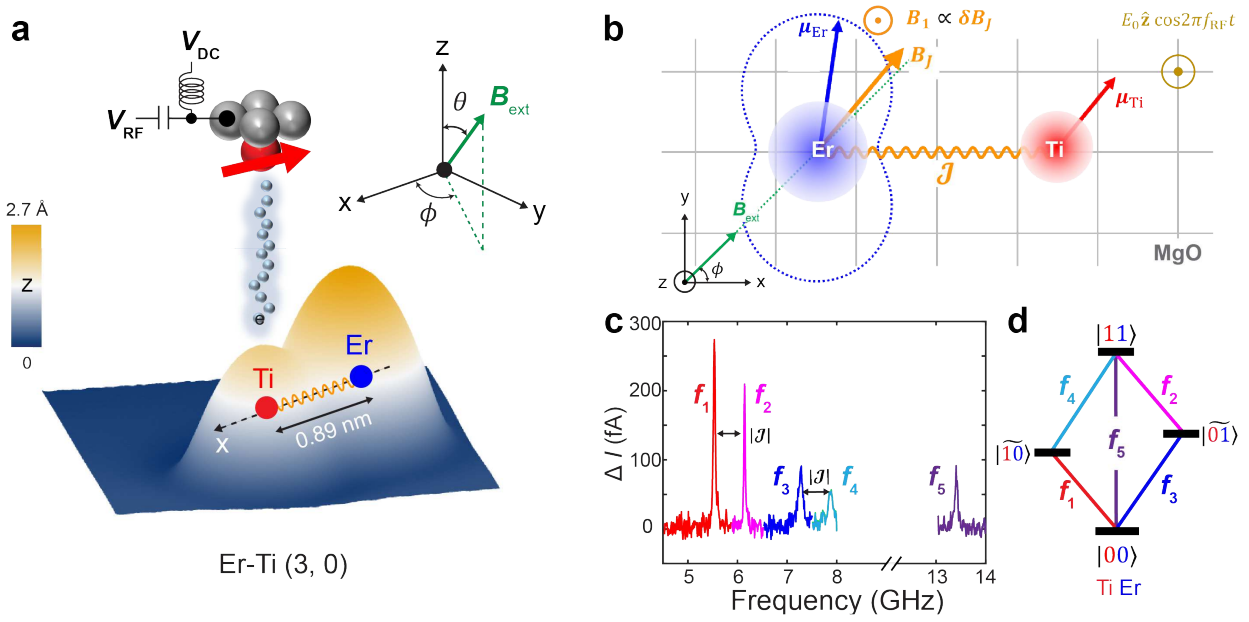


FIG. 1. **Schematics and ESR spectrum of an Er-Ti pair. a,** Schematic and three-dimensional STM topograph of an Er-Ti pair oriented along the O-O direction on MgO, 3.0 nm × 3.0 nm. The gray cylinder indicates the tunneling current, with the small gray balls representing the tunneling electrons. **b,** Schematic of an Er-Ti spin pair along the O-O direction on MgO, coupled by the spin-spin interaction $\mathcal{J}$. Owing to the anisotropic $\mathfrak{g}$-tensors, the magnetic moments of Ti and Er, $\boldsymbol{\mu}_{\rm Ti}$ and $\boldsymbol{\mu}_{\rm Er}$, are generally noncollinear with $\boldsymbol{B}_{\rm ext}$. The peanut-shaped blue dashed line shows a representative anisotropic magnetic moment of Er for the situation of $\mathfrak{g}_{yy}^{\rm Er} \sim 2\mathfrak{g}_{xx}^{\rm Er}$. The nearby Ti spin generates an effective exchange field ($\boldsymbol{B}_{\mathcal{J}}$) acting on Er; its RF-induced modulation provides a transverse driving field, $\boldsymbol{B}_1 \propto \delta\boldsymbol{B}_{\mathcal{J}}$, for Er spin transitions. The RF electric field is applied along the z-axis. The gray lines indicate the MgO lattice, with intersections marking oxygen atomic sites. The surface lattice constant is defined by the nearest-neighbor O-O distance. **c,** Representative ESR spectrum of the Er-Ti pair measured at $\boldsymbol{B}_{\rm ext} = 0.25$ T, $\theta = 83°$, and $\phi = 52°$. **d,** Energy-level diagram of the Er-Ti spin pair. Unless otherwise noted, all data were taken at $V_{\rm DC} = 100$ mV, $I_{\rm DC} = 20$ pA, and $T = 1.0$ K. The data in (**c**) were acquired with $V_{\rm RF} = 20$ mV.

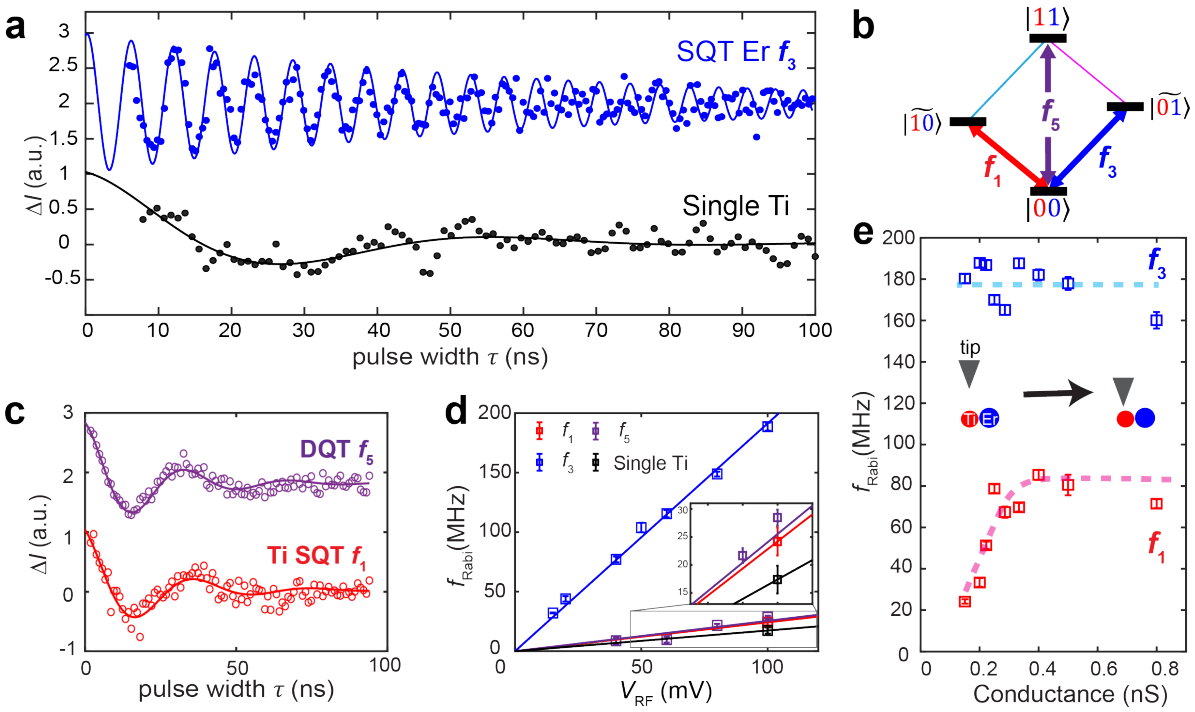


FIG. 2. **Coherent control of the Er spin. a,** Rabi oscillations of the f_3 transition ($f_{\rm res}$ = 7.28 GHz) in the pair and in a single Ti spin on the same surface. Both datasets were taken using the same tip with $V_{\rm DC}$ = 100 mV, $I_{\rm DC}$ = 20 pA. The solid lines are fits to exponentially decaying sinusoids. **b,** Energy diagram under this field condition where $|\pm\rangle$ are approximately Zeeman product states: $|\widetilde{01}\rangle$ and $|\widetilde{10}\rangle$. **c,** Rabi oscillations of f_1 and f_5 with the solid lines showing fits to exponentially decaying sinusoids. **d,** Rabi frequency as a function of $V_{\rm RF}$. Inset shows a magnified view of Rabi frequency vs $V_{\rm RF}$ specifically for f_1 ($f_{\rm res}$ = 5.55 GHz) and f_5 ($f_{\rm res}$ = 13.44 GHz). **e,** Rabi frequency of f_3 (blue squares) and f_1 (red squares) as a function of the conductance. The dashed cyan lines are guides to the eye. All data except in (**e**) were taken with a junction condition of $V_{\rm DC}$ = 100 mV, $I_{\rm DC}$ = 20 pA, $\boldsymbol{B}_{\rm ext}$ = 0.25 T, θ = 83°, ϕ = 52°. All data were acquired at 1.0 K.

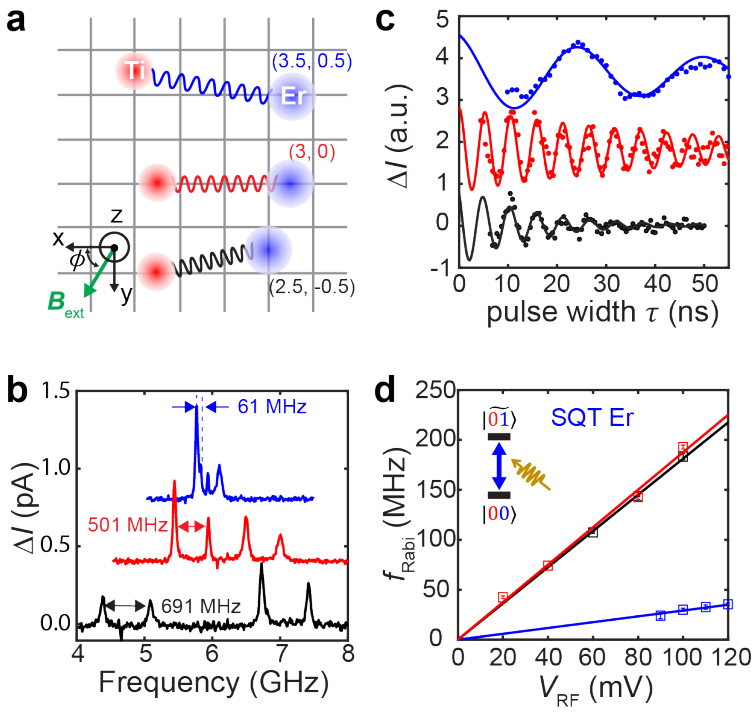


FIG. 3. **Pair engineering. a,** Schematics for three different pairs. The gray grid represents the MgO lattice with oxygen sites at the intersections. **b,** ESR spectra of the three pairs taken at $\boldsymbol{B}_{\rm ext} = 0.25$ T, $\phi = 52°$ and $\theta = 90°$. The interaction increases from 61 MHz to 691 MHz with decreasing separation between two spins. **c,** Rabi oscillations of f_3 (Er transition) in each pair ($V_{\rm RF} = 100$ mV, $f_{\rm res} = 6.10$ GHz for (3.5, 0.5) pair, $f_{\rm res} = 6.40$ GHz for (3, 0) pair, and $f_{\rm res} = 4.38$ GHz for (2.5, −0.5) pair). **d,** Rabi frequency of f_3 in each pair as a function of $V_{\rm RF}$. All data were taken with $V_{\rm DC} = 100$ mV and $I_{\rm DC} = 20$ pA at 1.0 K.

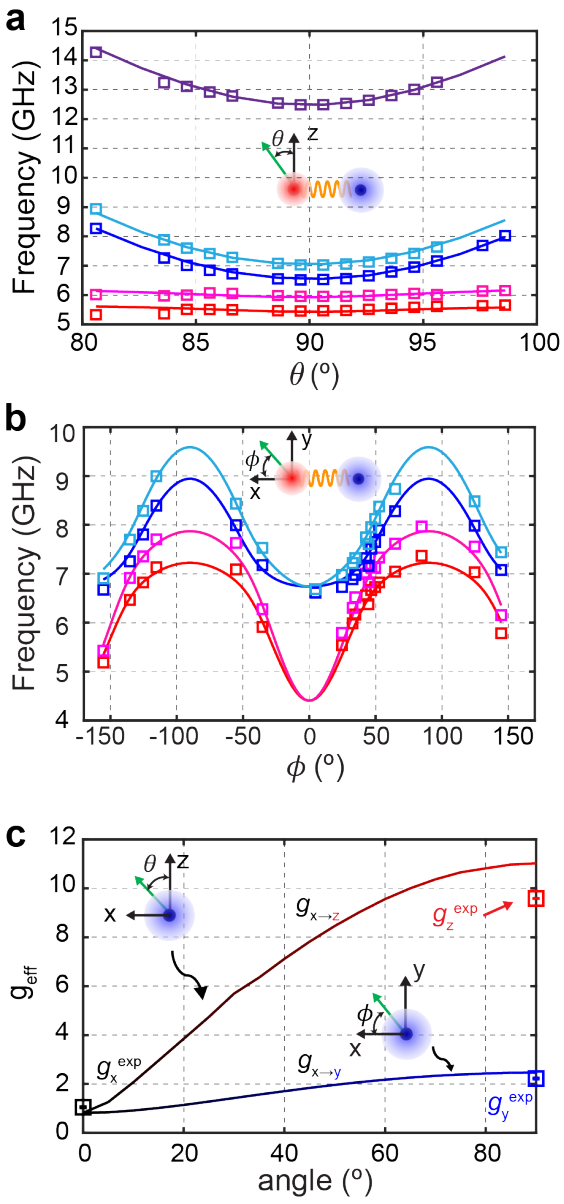


FIG. 4. **Magnetic anisotropy of the Er-Ti (3, 0) pair. a,** ESR transition energy as a function of the polar angle θ of $\boldsymbol{B}_{\rm ext}$ with ϕ fixed at 52°. **b,** ESR transition energy as a function of the azimuthal angle ϕ of $\boldsymbol{B}_{\rm ext}$ ($\theta = 90°$). Data in (**a**) were taken with $V_{\rm RF}$ = 20 mV, $V_{\rm DC}$ = 100 mV, $I_{\rm DC}$ = 20 pA and $\boldsymbol{B}_{\rm ext}$ = 0.25 T. Data in (**b**) were taken with $V_{\rm RF}$ = 20 mV, $V_{\rm DC}$ = 50 mV, $I_{\rm DC}$ = 20 pA and $\boldsymbol{B}_{\rm ext}$ = 0.3 T. **c,** The principal values of $\mathfrak{g}$-tensor from multiplet calculation (solid lines) and fitting of experimental data (colored squares). The solid lines show how the principal values of the $\mathfrak{g}$-tensor change as a function of θ and ϕ (see insets). All data were taken at 1.0 K.

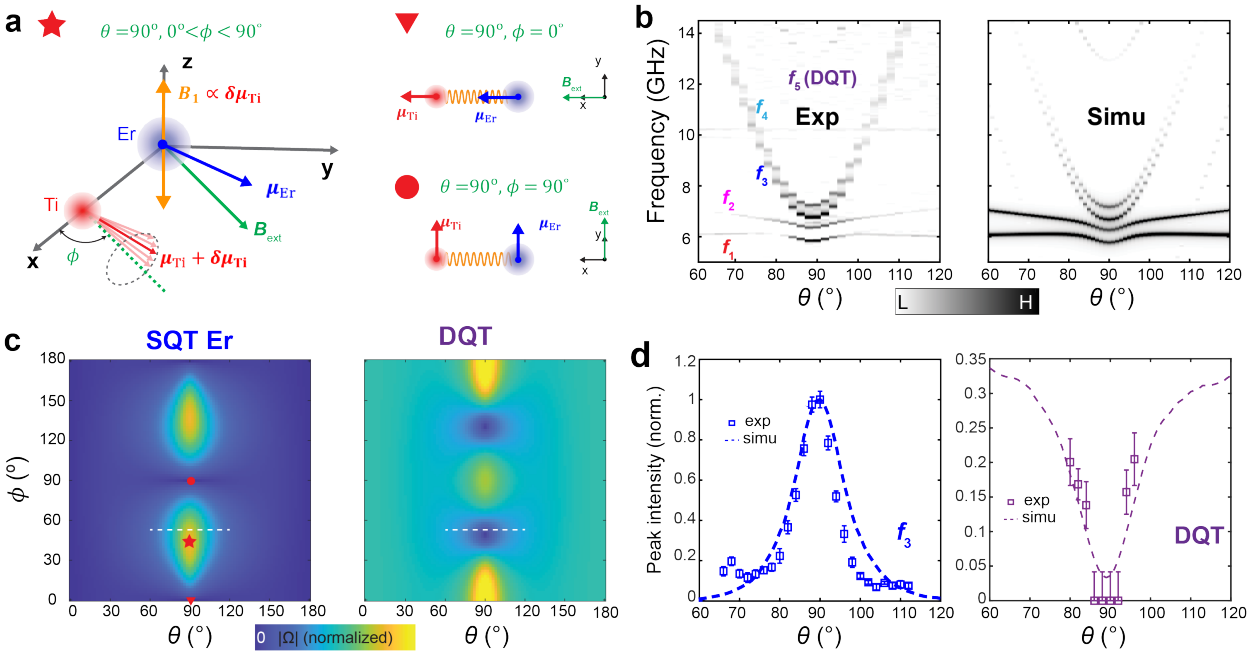


FIG. 5. **Coherent control mechanism. a,** Schematics of coherent control mechanism for special cases of $\theta = 90°$ and $0° < \phi < 90°$ (left panel), $\theta = 90°$ and $\phi = 0°$ (upper-right panel) and $\theta = 90°$ and $\phi = 90°$ (lower-right panel), corresponding to the markers in (**c**). When $\theta = 90°$ and $0° < \phi < 90°$, the Er and Ti magnetic moments are tilted away from $\boldsymbol{B}_{\rm ext}$ toward the y axis. The wobbling of the Ti magnetic moment around $\boldsymbol{B}_{\rm ext}$ periodically generates an out-of-plane component of the Ti moment, as illustrated in Fig. 1**b**. Through the anisotropic interaction, this produces an out-of-plane effective field, which is strongly amplified by the large $\mathfrak{g}_{zz}^{\rm Er}$ and appears as a transverse driving field for Er spin. When $\theta = 90°$ and $\phi = 0°$ or $\phi = 90°$, the spins are aligned with $\boldsymbol{B}_{\rm ext}$ and therefore the wobbling of magnetic moments does not generate any effective field driving single spin transitions. **b,** Experimental and simulated ESR maps as a function of the polar angle θ at $\phi = 52°$ and $\boldsymbol{B}_{\rm ext} = 0.25$ T. The simulation is based on rotational modulation within a Lindblad formalism (Supplementary Section X). **c,** Simulated Rabi frequency maps based on rotational modulation for the Er SQT (left) and the DQT (right). **d,** ESR intensities of f_3 and the DQT as a function of the θ. Dashed lines correspond to simulated results in (**b**) and colored squares denote experimental data. All data were acquired at $T = 1.0$ K with $V_{\rm DC} = 100$ mV, $I_{\rm DC} = 20$ pA, and $V_{\rm RF} = 20$ mV. The experimental data in (**b, d**) correspond to the ϕ angle indicated by the dashed white lines in (**c**).

Supplementary Files

This is a list of supplementary files associated with this preprint. Click to download.

- ErCoherentControlSI.pdf